Microchimica Acta (2019) 186: 819
https://doi.org/10.1007/s00604-019-3798-6

ORIGINAL PAPER

A voltammetric sensor for simultaneous determination of hydroquinone and catechol by using a heterojunction prepared from gold nanoparticle and graphitic carbon nitride

Hua Guo[1] · YanLing Shen[1] · Huiying Ouyang[1] · Yumei Long[1,2] · Weifeng Li[1]

Received: 1 April 2019 / Accepted: 7 September 2019 / Published online: 20 November 2019

Abstract

An electrochemical sensor is described for the simultaneous determination of hydroquinone (HQ) and catechol (CC) based on a nanocomposite consisting of gold nanoparticles and graphitic carbon nitride (g-C_3N_4). The nanocomposite was synthesized via one-step thermal polymerization route and characterized by X-ray diffraction, transmission electron microscopy, and Fourier transform infrared techniques. The results confirmed the close contact between gold nanoparticles and g-C_3N_4. The nanocomposites exhibited the enhanced electrocatalytic redox towards HQ and CC. A glassy carbon electrode was modified with the nanocomposite to obtain a sensor that exhibited favorable analytical properties in the simultaneous detection of HQ and CC, with voltammetric peaks typically near −0.14 and − 0.02 V (vs. saturated calomel electrode). Linear responses are found between 1.0 and 320 μM for HQ (with a 0.3 μM detection limit; at S/N = 3), and between 0.1 and 320 μM for CC (with a 0.04 μM detection limit; at S/N = 3). The sensor was applied for the simultaneous determination of HQ and CC in spiked water samples, and acceptable recoveries were achieved. The superior sensing properties of the electrode are attributed to the synergy between the microstructure (heterojunction and porosity) and the π interactions between phenolic isomers and g-C_3N_4.

Keywords Heterostructure · Simultaneous determination · Phenolic isomers · Single-source precursor · Electrochemistry · Electrocatalysis

Introduction

Hydroquinone and catechol are widely used in dyes, cosmetics, plastic, agricultural chemicals and medicine fields [1]. However, they can cause harm to human health even at very low concentration. Besides, HQ and CC are difficult to degrade in the ecological environment [2]. Thereby, both HQ and CC are considered as priority environmental pollutants by the US Environmental Protection Agency (EPA) and the European Union (EU) [3]. HQ and CC usually interfere with each other when assayed, this resulting from their similar structures and performance [4]. Thus, development of a rapid and effective method to simultaneously determine such two isomers remains a challenge.

Many analytical techniques have been developed to detect HQ and CC. These methods include gas chromatography/mass spectrometry (GC-MS) [5], high performance liquid chromatography (HPLC) [6], UV-Vis absorption spectrum [7], and chemiluninescence [8]. However, most of these methods are time-consuming, require complicated operation procedures and expert technical skill, which limit their routine analysis. Electrochemical sensor has intrigued tremendous interest in terms of its advantages, such as high sensitivity, good selectivity, easy operation and in situ analysis [9, 10]. As is well known, the performance of an electrochemical sensor is dependant on the electro-catalytic ability of modifing

Electronic supplementary material The online version of this article (https://doi.org/10.1007/s00604-019-3798-6) contains supplementary material, which is available to authorized users.

✉ Yumei Long
yumeilong@suda.edu.cn

✉ Weifeng Li
liweifeng@suda.edu.cn

[1] College of Chemistry, Chemical engineering and Materials Science, Soochow University, Suzhou, Jiangsu 215123, People's Republic of China

[2] The Key Lab of Health Chemistry and Molecular Diagnosis of Suzhou, Soochow University, Suzhou, Jiangsu 215123, People's Republic of China

materials [11, 12]. Therefore, much endeavor has been performed on searching for new nanomaterials with high electroactivity.

Graphitic carbon nitride (g-C_3N_4) is a fascinating organic semiconductor and has potential applications in photocatalyst and sensing fields [13–16]. However, the poor electrical conductivity and slow electron migration rate of native g-C_3N_4 led to its weak catalytic activity. To overcome these drawbacks, formation of heterojunction between g-C_3N_4 and other compounds (semiconductors or metals) has been proved to be an efficient way [17, 18]. The efficient heterojunction formed by chemically distinct components can trap carriers and mediate their transport properties, regulating the photoelectrochemical properties of semiconductors [19, 20]. For example, through hybridizing with metal nanomaterials, g-C_3N_4 was endowed with good electrocatalytic activity [21, 22].

In this work, gold/g-C_3N_4 nanocomposites were prepared using a single-source precursor modified from previous work [23]. Thanks to its good electrocatalytic activity towards dibydroxybenzene isomers, a novel electrochemical sensor was constructed for the simultaneous detection of HQ and CC. As is expected, the electrochemical sensor exhibited excellent analytical properties and consequently, was applied for real sample determination.

Experimental

Chemicals

The information about chemicals used in this work can be found in Electronic Supplementary Material.

Preparation of Au/g-C_3N_4 nanocomposite

Gold/g-C_3N_4 was prepared modified from our previous work [23], as illustrated in Fig. S1. Typically, 3.0 g of melamine and 0.03 g of chloroauric acid tetrahydrate were dissolved into 100 mL hot water (80 °C). Its pH was adjusted to 6.5. Next, the mixture was transferred into a rotary instrument to further react at 80 °C for 3 h. After that, orange precipitate was collected and dried at 80 °C overnight. Finally, the precursor was subjected to thermal condensation at 550 °C along with active carbon for 2 h. The products were purple color and they were grounded into powder.

Fabrication of modified glassy carbon electrodes

Prior to use, a GCE (3 mm in diameter) was polished with 1.0, 0.3, and 0.05 μm alumina slurries in sequence (Aida Hengsheng Co. Ltd., Tianjin, China http://www.tjaida.cn/). After each polishing, the GCE was sonicated in ethanol and de-ionized water for 10 min. Secondly, the electrode was electrochemically pretreated in H_2SO_4 aqueous solution (1.0 M) and in de-ionized water, respectively. The cycling potential was set between −1.0 and 1.0 V at a scan rate of 100 $mV \cdot s^{-1}$. After dried in a flow of nitrogen, 20 μL of the Au/g-C_3N_4 suspension (1 $mg \cdot mL^{-1}$ in ethanol) was drop-coated onto the surface of the GCE. Then, the mosified GCE was carefully rinsed with water to remove the unbounded substances and dried overnight at RT. The modified electrode was named as Au-g-C_3N_4/CCE. For a control experiment, g-C_3N_4 modified GCE was also constructed.

Apparatus

XRD patterns were collected on a PANalytical X-Pert-Pro MPD x-ray diffractometer with Cu-$K_{\alpha 1}$ radiation (Netherlands, https://www.panalytical.com.cn/). The size and morphologies of products were characterized by scanning electron microscopy (SEM, Hitachi S-4600, Japan, https://www.hitachi.com.cn/) and TEM (FEI Tecnai G20 F20 S-TWIN 200 KV, USA, http://www.fei.com/). FT-IR spectroscopy was obtained on a Nicolet 550 spectrometer (Varian, USA, https://www.varian.com). Elements of the samples were determined by x-ray photoelectron spectroscopy (XPS, Axis Ultra HAS with Al-K_α radiation, https://corporate.thermofisher.com). The surface area was determined by Brunauer-Emmett-Teller (BET) model using the N_2 adsorption/desorption isotherm, recorded on a Micromeritics ASAP2020 system (Micromeritics, USA, http://www.micromeritics.com.cn) at liquid nitrogen temperature. The gold concentration in the Au/g-C_3N_4 composite was determined using thermogravimetric (TG) technique (TG/DTA 6300, Japan, http://www.nsk.com/jp).

Cyclic voltammetry (CV) measurements were performed with a CHI611D electrochemical workstation (Chenhua Instruments Co., China, http://www.chinstr.com/). The CV measurements were based on a conventional three-electrode system, which includes a platinum electrode (counter electrode), a saturated calomel electrode (SCE, reference electrode), and a modified electrode (working electrode). CVs were recorded in the range from −1.0 to 1.0 V. Electrochemical impedance spectroscopy (EIS) was performed on a RST5200 electrochemical workstation (Suzhou Risetest Instrument Co. LTD., China, http://www.rst0000.com/). The supporting electrolyte was 0.1 M of KCl solution containing 1 mM $[Fe(CN)_6]^{3-/4-}$ (1:1) mixture.

Results and discussion

Choice of materials

G-C_3N_4 has received extensive attention due to its potential applications as catalyst and sensing material [13, 14].

Unfortunately, the application of pristine of g-C_3N_4 is limited by its low quantum efficiency and small surface area. Formation of heterojunction has shown to notably improve its photoelectrochemical performance. Because of its beneficial role as electron trap and co-catalytst, AuNP can act as sensitizer to improve photoelectric properties of semiconductors [24–26]. However, AuNPs are easy to aggregate, and thus needed to be stabilized by surfactants, which will reduce their optoelectric properties. On the other hand, g-C_3N_4-based heterostructures were mostly obtained by physically mixing with further heat-treatment. Such multistep processes cannot ensure the thorough blending at molecular level. As a result, the enhancement of electron transport is restricted because of the inefficient interface between g-C_3N_4 and the reinforcement compounds. Therefore, the achievement of efficient heterojunction between nanosized building blocks is a prerequisite for maximizing the potential of nanocomposites.

Characterization of Au/g-C_3N_4

The formation of single-source precursor of melamine chloroauric is evidenced by FTIR (Fig. S2). For melamine, the absorption bands in the range of 3000~3500 and 1600~1700 cm^{-1} are originated from vibration modes of amine groups. The peaks in the range between 800 and 1600 cm^{-1} correspond to vibration of triazine ring [27]. The precursor sample has the similar FTIR curve to that of melamine, indicating that the combination of $[AuCl_4]^-$ did not change its primary structure. Significantly, several new absorption peaks appear at 1510 and 1602 cm^{-1} (rectangle in Fig. S2), which should be caused by the protonated melamine [27].

Figure 1a shows the XRD patterns of the products. For both g-C_3N_4 and Au/g-C_3N_4 samples, two characteristic peaks at 27.4 ° and 13.0 ° are clearly observed, which are corresponded to (002) interlayer stacking and (100) in-plane packing of tri-s-triazine units, respectively [16]. Besides, several new diffraction peaks at 38 °, 44.4 °, 64.5 °, and 77.5 ° can be found in Au/g-C_3N_4. They are ascribed to the (111), (200), (220), and (311) planes of cubic-phase v (PDF # 98–000-0230), respectively [28]. The XRD results suggest the successful hybridization of g-C_3N_4 with gold nanoparticles.

Figure 1b presents FTIR spectra of g-C_3N_4 and Au/g-C_3N_4. Both the FTIR spectra exhibit characteristic absorption peaks for graphitic type of carbon nitride, indicating that the introduction of AuNPs does not change the chief chemical skeleton of g-C_3N_4. However, several absorption peaks (corresponding to C-N vibrations) of Au/g-C_3N_4 shift to high wavenumber compared to those of g-C_3N_4 [29]. For example, the 1237 shifts to 1245 cm^{-1} and the 1407 shifts to 1413 cm^{-1}. This phenomenon is attributed to the strong interaction between g-C_3N_4 and gold nanoparticles.

Fig. S3 shows XPS of samples. The survey XPS (Fig. S3A) reveals that both the samples are chiefly composed of carbon and nitrogen. The weak O 1 s peak at 532 eV origins from the adsorbed water. Different from that of g-C_3N_4, a weak XPS peak at 83 eV is appeared for Au/g-C_3N_4 sample. Fig. S3B presents the high-solution XPS of gold. Two peaks are found at 86.8 and 83.0 eV, which are assignable to $4f_{5/2}$ and $4f_{7/2}$ of Au^0, respectively [28]. The XPS results confirm the combination between gold and g-C_3N_4. Fig. S3C shows two peaks at 284.5 eV and 288.1 eV. They are related to the graphitic carbon and the sp^2-bonded carbon in N=C-N of g-C_3N_4, respectively. For N element (Fig. S3D), the binding energy of N 1 s in Au/g-C_3N_4 sample changes as compared to that in g-C_3N_4, revealing that their chemical environment has been affected. It is the fact that the delocalized π bond of g-C_3N_4 with high electron density provides lone-pair electrons to the d orbit of Au.

The microstructures of samples were observed by SEM and TEM techniques. Figure 2a, b show SEM images of samples. Pure g-C_3N_4 shows aggregated morphology with large size (Fig. 2a). After AuNPs loading, the size of g-C_3N_4 becomes small. Furthermore, the g-C_3N_4 is corroded and many irregular pores appear (Fig. 2b), indicating that the introduction of gold exerts great influence on the microstructure of g-C_3N_4. In the case of melamine chloroauric, the produced AuNPs can catalyze and promote the decomposition of

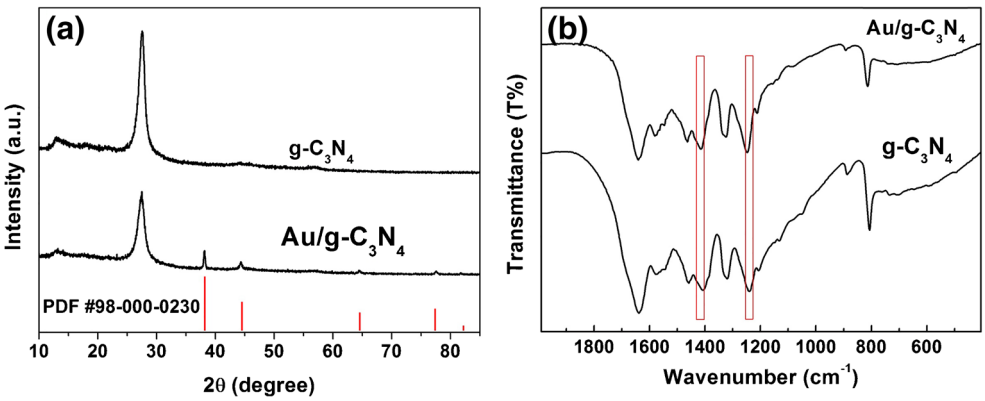

Fig. 1 **a** XRD patterns and **b** FT-IR spectra of g-C_3N_4 and Au/g-C_3N_4 samples

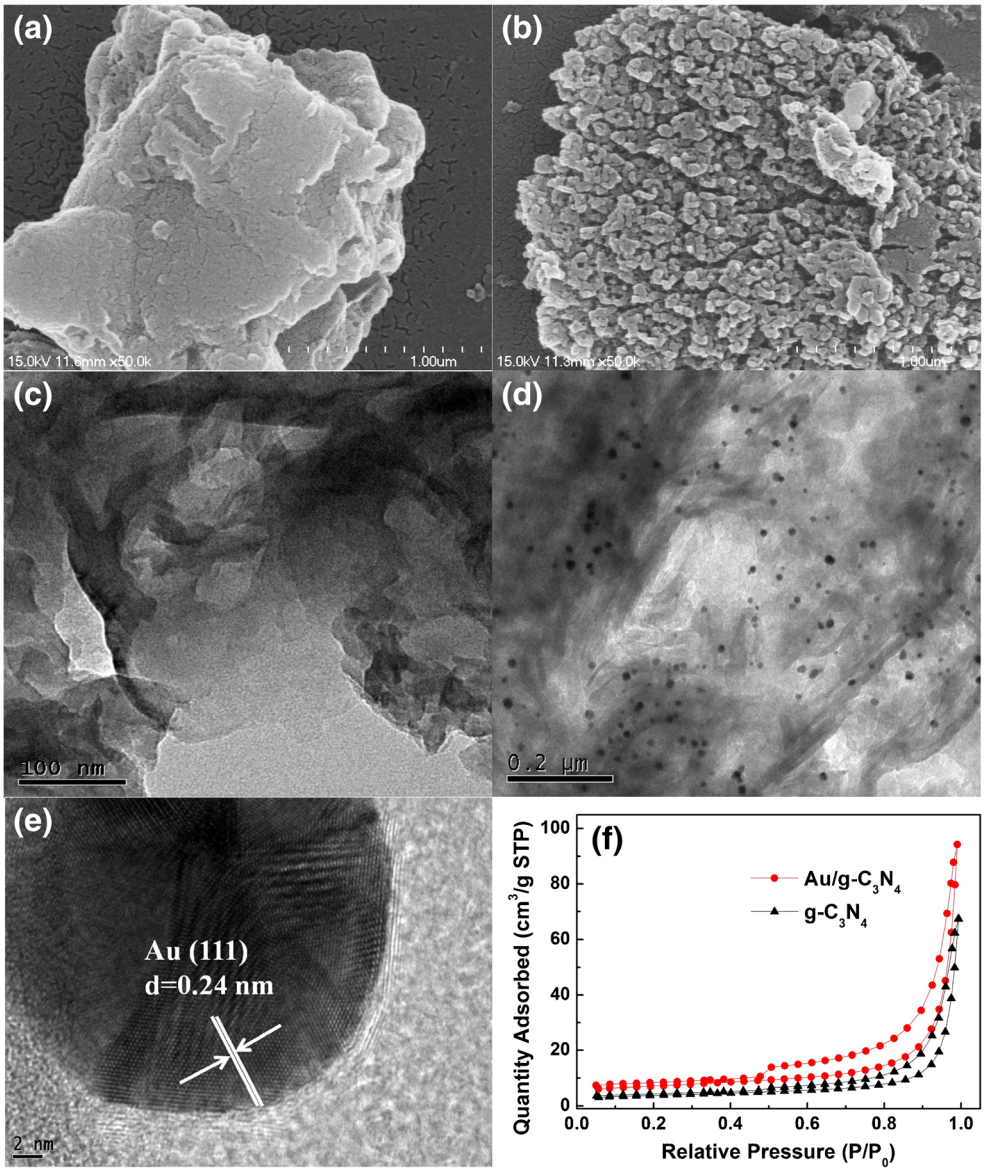

Fig. 2 SEM images of (**a**) g-C_3N_4 and (**b**) Au-g-C_3N_4; TEM images of (**c**) g-C_3N_4 and (**d**) Au-g-C_3N_4; (**e**) High-magnification TEM image of Au-g-C_3N_4 nanocomposites; and (**f**) N_2 adsorption-desorption isotherms of pure g-C_3N_4 and Au/g-C_3N_4 nanocomposite

precursor to release more gases during the pyrolyzation process. It is corroborated by the smaller yield of Au/g-C_3N_4 (about 12%) compared to that of pure g-C_3N_4 (about 46%). These gases not only prevent the aggregation of g-C_3N_4 particles, but also act as a foaming agent to achieve the porous structure of Au/g-C_3N_4. The EDS result (Fig. S4) suggests that the Au/g-C_3N_4 is composed of C, N and Au elements. Based on the excellent thermostability of gold and thermal decomposition of g-C_3N_4 at high temperature, the gold content was determined by TG analysis (Fig. S5). Thus, the gold content is estimated to be 3.48 wt% in Au/g-C_3N_4.

The combination between AuNPs and g-C_3N_4 is further evidenced by TEM, as shown in Fig. 2c, e. The g-C_3N_4 shows sheet-like structure with large size and these layers are aggregated (Fig. 2c). For Au/g-C_3N_4 nanocomposite, AuNPs (dark particles) are clearly observed on the surface of g-C_3N_4 and they are in close contact (Fig. 2d), indicating the co-existence of AuNPs and g-C_3N_4. The HRTEM image of Au/g-C_3N_4 (Fig. 2e) illustrates a clear inter-fringe, whose space distance is about 0.24 nm. The value marches well with (111) plane of cubic gold [28]. Around AuNPs, there exists light color part without lattice spacings. It represents g-C_3N_4. The transition region between g-C_3N_4 and AuNPs is smooth, suggesting the close contact between AuNPs and g-C_3N_4 [30]. The close attachment of AuNPs on the surface of g-C_3N_4 is ascribed to the fact that AuNPs and g-C_3N_4 are produced from the same precursor. Therefore, the single-source precursor strategy renders the uniform distribution of AuNPs on g-C_3N_4, as well as strong interaction between them. It is beneficial to bringing the synergy between AuNPs and g-C_3N_4 into full play. Figure 2f gives the N_2 adsorption-desorption isotherms of g-C_3N_4 and Au/g-C_3N_4. Based on the BET analysis, the surface

area of Au/g-C_3N_4 (23.7 $m^2 \cdot g^{-1}$) is larger than that of g-C_3N_4 (12.9 $m^2 \cdot g^{-1}$). This result is consistent with the SEM observation on porous structure of Au/g-C_3N_4 sample (Fig. 2b).

Electrochemical behavior of the modified glassy carbon electrodes

Figure 3 shows the dependence of CVs on the scan rates for the Au-g-C_3N_4/GCE and g-C_3N_4/GCE. For both the electrodes, redox peak current enhance with increasing scan rate (Fig. 3a, c). There are good linear relationships between the peak current intensity and the square root of scan rate (Fig. 3b, d). According to Randles-Sevcik eq. [31],

$$I_p = 2.69 \times 10^5 \cdot n^{3/2} \cdot S \cdot D^{1/2} \cdot C \cdot \upsilon^{1/2} \quad (1)$$

where I_p, S and υ are peak current, electrochemical active surface area (EASA, cm^2) and scan rate, respectively. Other symbols have specific physical meaning and they are constants here. Thus, the EASA of Au-g-C_3N_4/GCE was calculated to be 0.1918 cm^2, which is larger than that of g-C_3N_4/GCE (0.1751 cm^2). The large EASA of Au-g-C_3N_4/GCE can improve its current response.

Fig. S5 illustrates Nyquist plots at different electrodes measured in 0.1 M KCl solution, in which $[Fe(CN)_6]^{3-/4-}$ (1 mM) was used as an electrochemically active prober. All the electrodes show the similar EIS curves, including a semicircular section and a linear section. The semicircular diameter is related to the electron transfer resistance (R_{et}), while the linear section reflects diffusion process. The R_{et} of bare GCE is about 400.6 Ω. After modification, the R_{et} values of the electrodes obviously increases. The large R_{et} should attributed to the semiconductor property of g-C_3N_4, which restricts the electron transfer between $[Fe(CN)_6]^{3-/4-}$ and electrode surface. Interestedly, the R_{et} at Au-g-C_3N_4/GCE (2773 Ω) is much smaller than that at g-C_3N_4/GCE (4751 Ω), indicating the enhanced transfer efficiency g-C_3N_4 by AuNPs decorating. The good electron transfer efficiency of Au/g-C_3N_4 should be ascribed to the large surface area of Au-g-C_3N_4 and the good conductivity of AuNPs.

Figure 4a shows CVs of bare, g-C_3N_4-, AuNPs-, and Au-g-C_3N_4-modified GCE in the presence of HQ and CC with scan rate of 100 $mV \cdot s^{-1}$. When 200 μM of HQ and 200 μM of CC were introduced into the PB solution (pH = 9), two well-separated cathodic peaks are observed for all the electrodes. Both the peaks (E_{pc}) at about −0.14 V and − 0.02 V are ascribed to the cathodic peaks (E_{pc}) of HQ and CC, respectively. However, only one broad anodic peak can be discerned in the reverse scaning, which is attributed to the overlapping between two oxidation peaks of CC and HQ under such a condition. Furthermore, the modified electrodes exhibit the increased redox currents and the Au-g-C_3N_4/GCE show the best current response. Thus, the synergic effect between AuNPs and g-C_3N_4 is evidenced. Firstly, the single-source precursor synthesis method endows heterostructure with an efficient interface between g-

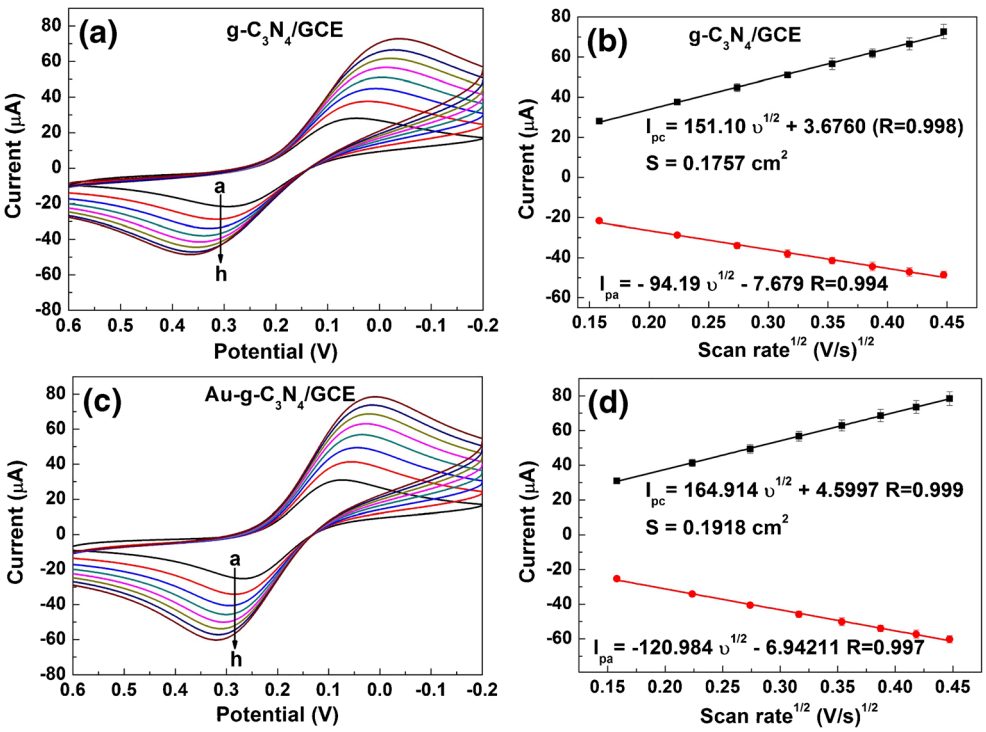

Fig. 3 **a** CVs at different scan rates: (a) 25, (b) 50, (c) 75, (d) 100, (e) 125, (f) 150, (g) 175 and (h) 200 $mV \cdot s^{-1}$, and **b** corresponding calibration plots between peak current and (scan rate)$^{1/2}$ of g-C_3N_4/GCE; **c** CVs at different scan rates: (a) 25, (b) 50, (c) 75, (d) 100, (e) 125, (f) 150, (g) 175 and (h) 200 $mV \cdot s^{-1}$, and **d** corresponding calibration plots between peak current and (scan rate)$^{1/2}$ of Au-g-C_3N_4/GCE. (Conditions: 0.1 M of KCl solution containing 1 mM $[Fe(CN)_6]^{3-/4-}$)

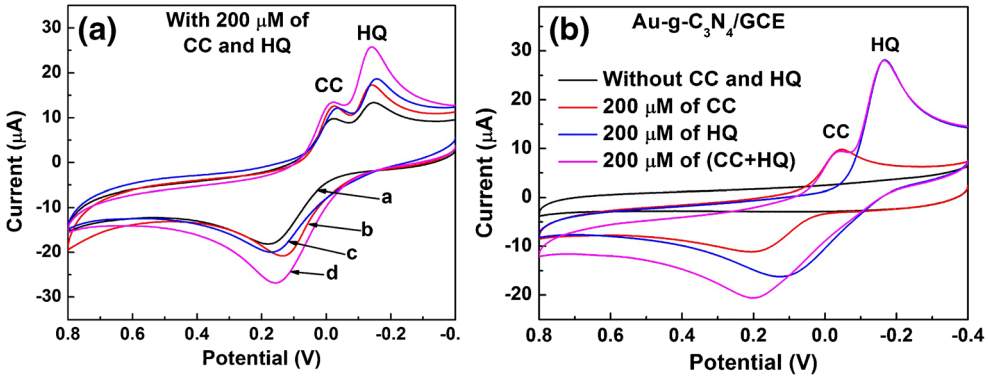

Fig. 4 **a** CVs of (a) bare GCE, (b) g-C_3N_4/GCE, (c) AuNPs/GCE and (d) Au-g-C_3N_4/GCE in the PB solution (pH = 9) with HQ (200 μM) and CC (200 μM); **b** CVs of Au-g-C_3N_4/GCE in the absence/presence of HQ (200 μM) or CC (200 μM) alone and the mixture of HQ (200 μM) and CC (200 μM) in 0.1 M PB solution with pH of 9. Scan rate: 100 $mV \cdot s^{-1}$

C_3N_4 and AuNPs. The high-quality heterojunction can effectively improve the electro-catalytic activity by facilitating the charge-transport and electron transfer at the electrolyte/electrode interface. Secondly, the porous structure of Au/g-C_3N_4 is helpful to the mass diffusion in the inner electrode, accelerating the kinetics of the electro-catalytic reaction. Finally, the high BET surface area of Au/g-C_3N_4 will provide more active sites for target compounds to react. Especially, the peak potential separation (cathodic peak) between HQ and CC is about 120 mV for Au-g-C_3N_4/GCE. Therefore, Au/g-C_3N_4 modified GCE can be applied for the simultaneous detection of HQ and CC. Figure 4b presents CVs of Au-g-C_3N_4/GCE in the absence/presence of HQ (200 μM) or CC (200 μM) alone, as well as the mixture (200 μM HQ and 200 μM CC) in the 0.1 M PB soution (pH = 9). No current response is observed without CC and HQ. When HQ or CC was added into the PB soution, two well-defined cathodic peaks appear. HQ and CC have little impact on each other in the current response.

Optimization of method

In order to achieve good analytic performance of the sensor, the following parameters were optimized: (a) Scan rate and (b) sample pH value. Respective text and figures on optimizations are given in the Electronic Supporting Material. It was revealed that the sample pH value of 9 can give the best results.

Simultaneous detection of HQ and CC using au/g-C_3N_4/GCE sensor

Figure 5a shows the electrochemical response of Au-g-C_3N_4/GCE in the mixed solution when the concentrations of HQ and CC are simultaneously changed. With increasing the concentrations of HQ and CC, the redox peak current gradually enhance, while their peak potentials are hardly changed. Furthermore, the cathodic peak of HQ is well separated from that of CC. Thus, cathodic peak current is employed to simultaneously determine HQ and CC. as shown in Fig. 5b, the cathodic peak currents are linearly dependant on the analyte concentrations. Their corresponding linear regression equations are defined as follows:

$$I_{pc}(\mu A) = 0.092[HQ]\ (\mu M) + 6.848 \quad (R = 0.991, 1.0\text{-}320\ \mu M)$$
$$I_{pc}(\mu A) = 0.031[CC]\ (\mu M) + 2.823 \quad (R = 0.993, 0.1\text{-}320\ \mu M)$$

Accordingly, the detection limits of HQ and CC are estimated to be 0.3 and 0.04 μM (S/*N* = 3), respectively. The sensitivities of Au-g-C_3N_4/GCE are 0.48 and 0.16 $\mu A \cdot \mu M^{-1} \cdot cm^{-2}$ for HQ and CC, respectively.

Figure 5c depicts the CVs of the Au-g-C_3N_4/GCE in the mixed solution, in which the HQ concentration varies from 0.1 to 320 μM with the fixed CC content of 20 μM. The cathodic peak currents of HQ increase linearly with increasing its concentrations. On the other hand, the peak current of CC is hardly changed. It should be noted that the slopes of linear relationships are different between the low (0.1–110 μM) and high concentration ranges (110–320 μM) (Fig. 5d). At lower concentration, there are sufficient active sites in the surface of electrode for HQ to react, resulting in a larger slope. When the HQ concentration increased, the active sites in the surface of electrode reduced, leading to relative smaller slope. Similar results were also obtained for CC detection at the fixed HQ content (20 μM) (Fig. 5e). As shown in Fig. 5f, the cathodic peak currents are linearly proportional to CC concentrations ranged from 0.1 to 330 μM. These results suggest the feasibility of Au-g-C_3N_4/GCE for the simultaneous detection of HQ and CC. For comparison, the analytical properties of Au-g-C_3N_4/GCE method and some reported electrochemical methods in the detection of HQ and CC are summarized in Table S1. The Au-g-C_3N_4/GCE sensor is superior over most of the other electrochemical techniques in terms of the linear range and low detection limit.

Selectivity is one of the most important parameters for electrochemical sensors to apply for real sample assay. Therefore, the selectivity of Au-g-C_3N_4/GCE was tested by

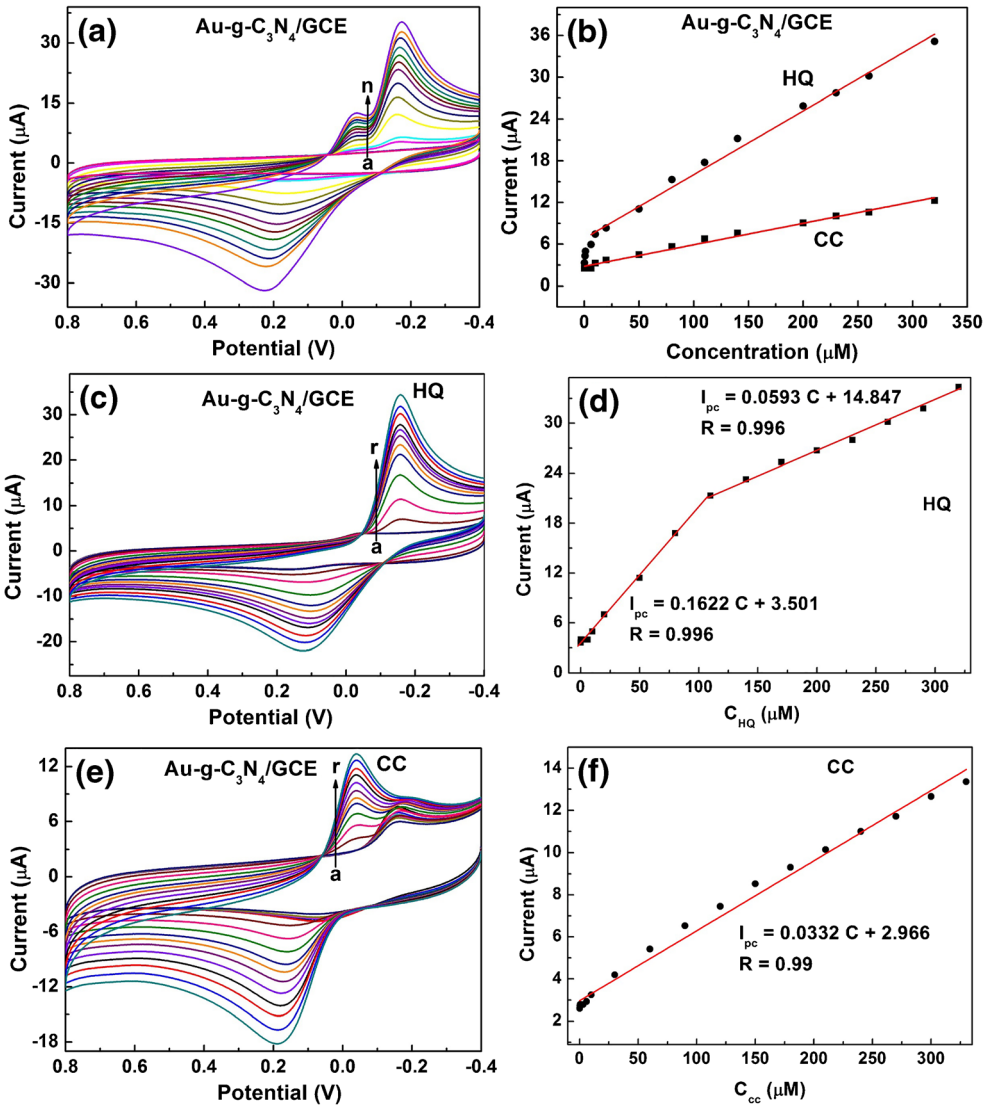

Fig. 5 **a** CVs of the Au-g-C_3N_4/GCE with successive additions of HQ and CC: (a) 0.1, (b) 0.6, (c) 1.0, (d) 6.0, (e) 10, (f) 20, (g) 50, (h) 80, (i) 110, (j) 140, (k) 200, (l) 230, (m) 260, (n) 320 μM; **b** calibration plots between peak current and concentration obtained by simultaneous analysis for HQ and CC; **c** CVs of the Au-g-C_3N_4/GCE for different HQ concentrations with fixed CC content of 20 μM: (a) 0.1, (b) 0.3, (c) 0.6, (d) 1.0, (e) 3.0, (f) 6.0, (g) 10, (h) 20, (i) 50, (j) 80, (k) 110, (l) 140, (m) 170, (n) 200, (o) 230, (p) 260, (q) 290 and (r) 320 μM; **d** calibration plots for HQ; **e** CVs of the Au-g-C_3N_4/GCE for different HQ concentrations with fixed CC content of 20 μM: (a) 0.1, (b) 0.3, (c) 0.6, (d) 1.0, (e) 3.0, (f) 6.0, (g) 10, (h) 30, (i) 60, (j) 90, (k) 120, (l) 150, (m) 180, (n) 210, (o) 240, (p) 270, (q) 300 and (r) 330 μM; **f** calibration plot for CC. (Conditions: 0.1 M of PB solution, pH = 9; scan rate: 100 $mV \cdot s^{-1}$)

measuring CVs of HQ (50 μM) and CC (50 μM) in the absence/presence of interfering species. These species are p-hydroxybenzoic acid (HBA, 50 μM), protocatechuic acid (PCA, 50 μM), uric acid (UA, 50 μM), ascorbic acid (AA, 50 μM), glucose (GLU, 2500 μM), KNO_3 (2500 μM), NaCl (2500 μM) and Na_2SO_4 (2500 μM). The CVs of HQ (CC) before and after the addition of interfering compounds are presented in Fig. 6. The relative errors induced by the investigated compounds are less than ±5%. Thus, the Au-g-C_3N_4/GCE possesses good selectivity towards HQ and CC. It was reported that the nitrogen functionalities in the Au/g-C_3N_4 nanocomposite will act as strong Lewis base sites to anchor phenolic isomers via special O-H···N or O-H···π interactions [32]. The π stacking interaction between g-C_3N_4 and benzene ring of phenolic isomers is also a significant factor. As a result, Au-g-C_3N_4/GCE exhibit good selectivity.

The operating repeatability of the sensor was evaluated by recording its current response towards HQ and CC (200 μM for each substance) through ten consecutive measurements (0.1 M PB solution, pH = 9). Their relative standard deviations (RSD) calculated by cathodic peak current are 2.49% for HQ and 1.37% for CC, respectively. Five Au-g-C_3N_4/GC electrodes were prepared in the same process and their current responses towards HQ and CC (200 μM for each substance) were measured (0.1 M of PB solution, pH = 9). The RSD values are estimated to be 3.85% and 6.18% for HQ and CC, respectively. The results reveal the good reproducibility of Au-g-C_3N_4/GC electrode. When not used, the Au-g-C_3N_4/GCE was stored in dry air at room temperature. After four weeks storage, the cathodic peak currents of the sensor decreased by about 11.09% for HQ and 5.39% for CC, as compared to their initial values. Thereby, Au-g-C_3N_4/GCE demonstrates excellent reproducibility and acceptable storage stability in the simultaneous detection of HQ and CC.

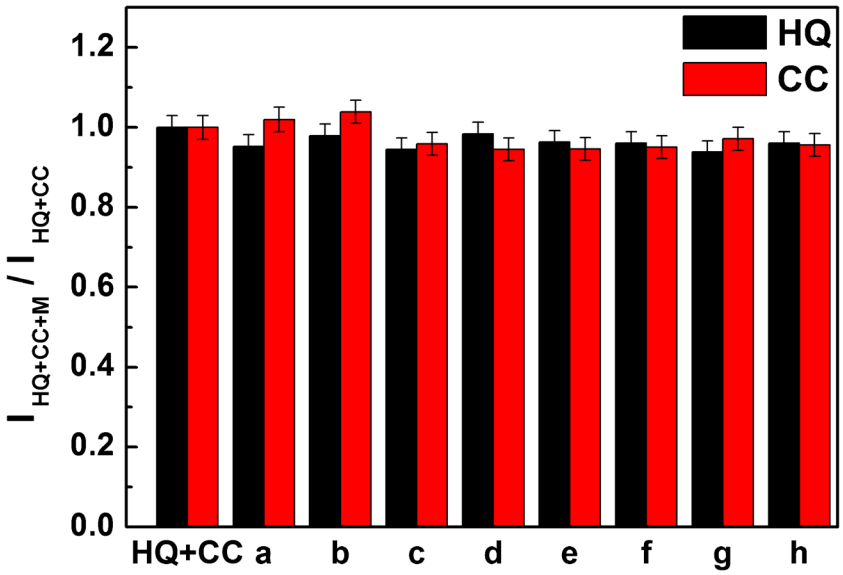

Fig. 6 The current response of HQ (50 μM, black) and CC (50 μM, red) on Au-g-C_3N_4/GCE in the presence of different interferences: 50 μM of p-hydroxybenzoic (a), protocatechuic acid (b), uric acid (c), ascorbic acid (d), and 2500 μM of Na_2SO_4 (e), KNO_3 (f), NaCl (g) and glucose (h). (Conditions: 0.1 M of PB solution, pH = 9; scan rate: 100 $mV \cdot s^{-1}$)

Real sample analysis

In view of its desirable analytical performance, the Au-g-C_3N_4/GCE was employed to detect HQ and CC in real samples, including tap water and lake water. The lake water was collected from Dushu Lake of Suzhou. Before analysis, the lake water was purified with a 0.45 μm millipore filter membrane (ϕ = 25 mm, Sangon Biotech Co., Ltd. China, https://www.sangon.com) to remove suspended solids. On the other hand, the tap water sample was used without any pretreatments. The measurement was performed using a standard addition method under the optimized conditions. Table 1 lists the recovery tests for the detection of HQ and CC in the real samples. The results reveal that the recovery values are in the range of 93.02–107.3% for HQ and 92.41–103.4% for CC, respectively. Thus, the sensor is effective for HQ and CC detection in real samples.

Conclusions

Gold nanoparticles g-C_3N_4 nanocomposite was synthesized using a single-source precursor. The Au/g-C_3N_4 heterostructure was employed to fabricate a novel electrochemical sensor for the simultaneous determination of HQ and CC. The Au-g-C_3N_4/GCE showed the enhanced electrocatalytic activity in the redox of HQ and CC, as compared with the other glassy carbon electrodes. The improved electrocatalytic performance was attributed to the synergic effect between AuNPs and g-C_3N_4. The results revealed that the sensor has excellent analytic properties in the simulataneous detection of HQ and CC. The detection limit of the Au-g-C_3N_4/GCE towards HQ and CC were estimated to be 0.3 and 0.04 μM, respectively. In addition, the reliable results were achieved when it was applied for real sample assay. It is believed that Au/g-C_3N_4 nanocomposite prepared from a single-source precursor can find more applications in sensor field.

Table 1 Simultaneous detection of HQ and CC in real samples using Au-g-C_3N_4/GCE

Sample	Add (μM)		Found (μM)		RSD (%) (n = 3)		Recovery (%)	
	HQ	CC	HQ	CC	HQ	CC	HQ	CC
Tap water	50.00	50.00	47.76	51.70	5.78	2.03	95.52	103.4
	100.0	100.0	94.80	92.41	2.84	1.43	94.80	92.41
	150.0	150.0	145.2	146.4	1.48	2.83	96.83	97.59
Dushu Lake water	50.00	50.00	53.65	51.63	2.00	2.77	107.3	103.3
	100.0	100.0	93.02	97.36	1.68	2.00	93.02	97.36
	150.0	150.0	142.8	149.6	1.62	1.36	95.22	99.75

Acknowledgements This work is supported by the National Natural Science Foundation of China (21005053), the Priority Academic Program Development of Jiangsu Higher Education Institutions and the Project of Scientific and Technologic Infrastructure of Suzhou (SZS201708).

Compliance with ethical standards

Conflict of interest The author(s) declare that they have no competing interests.

References

1. Huang KJ, Wang L, Liu YJ, Gan T, Liu YM, Wang LL, Fan Y (2013) Synthesis and electrochemical performances of layered tungsten sulfide-graphene nanocomposite as a sensing platform for catechol, resorcinol and hydroquinone. Electrochim Acta 10: 379–387. https://doi.org/10.1016/j.electacta.2013.06.060
2. Yuan X, Yuan D, Zeng F, Zou W, Tzorbatzogloub F, Tsiakaras P, Wang Y (2013) Preparation of graphitic mesoporous carbon for the simultaneous detection of hydroquinone and catechol. Appl Catal B Environ 129:367–374. https://doi.org/10.1016/j.apcatb.2012.09.017
3. Yang X, Kirsch J, Fergus J, Simonian A (2013) Modeling analysis of electrode fouling during electrolysis of phenolic compounds. Electrochim Acta 94:259–268. https://doi.org/10.1016/j.electacta.2013.01.019
4. Sun W, Wang YH, Lu YX, Hu AH, Shi F, Sun ZF (2013) High sensitive simultaneously electrochemical detection of hydroquinone and catechol with a poly (crystal violet) functionalized graphene modified carbon ionic liquid electrode. Sens Actuators B: Chem 188:564–570. https://doi.org/10.1016/j.snb.2013.07.032
5. Lourenco ELB, Ferreira A, Pinto E, Yonamine M, Farsky SHP (2006) On-Fiber derivatization of SPME extracts of phenol, hydroquinone and catechol with GC-MS detection. Chromatographia 63: 175–179. https://doi.org/10.1365/s10337-006-0719-80,009-5893/06/02
6. Marrubini G, Calleri E, Coccini T, Castoldi AF, Manzo L (2015) Direct analysis of phenol, catechol and hydroquinone in human urine by coupled-column HPLC with fluorimetric detection. Chromatographia 62:25–31. https://doi.org/10.1365/s10337-005-0570-30,009-5893/05/07
7. Song YW, Zhao MM, Li H, Wang XT, Cheng YF, Ding LJ, Fan S, Chen SG (2018) Facile preparation of urchin-like $NiCo_2O_4$ microspheres as oxidase mimetic for colormetric assay of hydroquinone. Sens Actuators B: Chem 255:1927–1936. https://doi.org/10.1016/j.snb.2017.08.204
8. Zhao LJ, Lv BQ, Yuan HY, Zhou ZD, Xiao D (2017) A sensitive chemiluminescence method for determination of hydroquinone and catechol. Sensors 7:578–588. https://doi.org/10.3390/s7040578
9. Liu LY, Ma Z, Zhu XH, Alshahrani LA, Tie SL, Nan JM (2016) A glassy carbon electrode modified with carbon nano-fragments and bismuth oxide for electrochemical analysis of trace catechol in the presence of high concentrations of hydroquinone. Microchim Acta 183:3293–3301. https://doi.org/10.1007/s00604-016-1973-6
10. Nasr B, Abdellatif G, Cañizares P, Sáez C, Lobato J, Rodrigo MA (2015) Electrochemical oxidation of hydroquinone, resorcinol, and catechol on boron-doped diamond anodes. Environ Sci Technol 39: 7234–7239. https://doi.org/10.1021/es0500660
11. Coroş M, Pogăcean F, Măgeruşan L, Roşu MC, Porav AS, Socaci C, Bende A, Staden RISV, Pruneanu S (2018) Graphene-porphyrin composite synthesis through graphite exfoliation: the electrochemical sensing of catechol. Sens Actuators B: Chem 256:665–673. https://doi.org/10.1016/j.snb.2017.09.205
12. Riskin M, Vered RT, Bourenko T, Granot E, Willner I (2008) Imprinting of molecular recognition sites through electropolymerization of functionalized Au nanoparticles: development of an electrochemical TNT sensor based on π-donor–acceptor interactions. J Am Chem Soc 130:9726–9733. https://doi.org/10.1021/ja711278c
13. Ong WJ, Tan LL, Ng YH, Yong ST, Chai SP (2016) Graphitic carbon nitride ($g\text{-}C_3N_4$)-based photocatalytsts for artificial photosynthesis and environmental remediation: are we a step closer to achieving sustainablility? Chem Rev. 116:7159–7329. https://doi.org/10.1021/acs.chemrev.6b00075
14. Sun YP, Ha W, Chen J, Qi HY, Shi YP (2016) Advances and applications of graphitic carbon nitride as sorbent in analytical chemistry for sample pretreatment: A review. TrAC Trends Anal Chem 84:12–21. https://doi.org/10.1016/j.trac.2016.03.002
15. Wu JJ, Li N, Fang HB, Li XT, Zheng YZ, Tao X (2019) Nitrogen vacancies modified graphitic carbon nitride: Scalable and one-step fabrication with efficient visible-light-driven hydrogen evolution. Chem Eng J 358:20–29. https://doi.org/10.1016/j.cej.2018.09.208
16. Wang XC, Maeda K, Thomas A, Takanabe K, Xin G, Carlsson JM, Domen K, Antonietti M (2008) A metal-free polymeric photocatalyst for hydrogen production from water under visible light. Nat Mater 8:76–80. https://doi.org/10.1038/nmat2317
17. Huang DL, Li ZH, Zeng GM, Zhou CY, Xue WJ, Gong XM, Yan XL, Chen S, Wang WJ, Cheng M (2019) Megamerger in photocatalytic field: 2D $g\text{-}C_3N_4$ nanosheets serve as support of 0D nanomaterials for improving photocatalytic performance. Appl Catal B: Environ 240:153–173. https://doi.org/10.1016/j.apcatb.2018.08.071
18. Masih D, Ma YY, Rohani S (2017) Graphitic C_3N_4 based noble-metal-free photocatalyst systems: A review. Appl Catal B: Environ 206:556–588. https://doi.org/10.1016/j.apcatb.2017.01.061
19. Zhang JT, Tang Y, Lee K, Ouyang M (2010) Nonepitaxial growth of hybrid core-shell nanostructures with large lattice mismatches. Science 327:1634–1638. https://doi.org/10.1126/science.1184769
20. Mamba G, Mishra AK (2016) Graphitic carbon nitride ($g\text{-}C_3N_4$) nanocomposites: A new and exciting generation of visible light driven photocatalysts for environmental pollution remediation. Appl Catal B: Environ 198:347–377. https://doi.org/10.1016/j.apcatb.2016.05.052
21. Zheng Y, Jiao Y, Zhu YH, Cai QR, Vasileff A, Li LH, Chen Y, Qiao SZ (2017) Molecule-level $g\text{-}C_3N_4$ coordinated transition metals as a new class of electrocatalysts for oxygen electrode reactions. J Am Chem Soc 139:3336–3339. https://doi.org/10.1021/jacs.6b13100
22. Jin J, Fu X, Liu Q, Zhang J (2013) A highly active and stable electrocatalyst for oxygen reduction reaction based on a grapheme-supported $g\text{-}C_3N_4$@cobalt oxide core-shell hybrid in alkaline solution. J Mater Chem A 1:10538–10,545. https://doi.org/10.1039/c3ta11144j
23. Guo H, Su Y, Shen YL, Long YM, Li WF (2019) In situ decoration of Au nanoparticles on carbon nitride using a single-source precursor and its application for the detection of tetracycline. J Colloid Interf Sci 536:646–654. https://doi.org/10.1016/j.jcis.2018.10.104
24. Ran JR, Jaroniec M, Qiao SZ (2018) Cocatalysts in semiconductor-based photocatalytic CO_2 reduction: achievements, challenges, and opportunities. Adv Mater 30:201704649. https://doi.org/10.1002/adma.201704649
25. Xu L, Ling SY, Li HN, Yan PC, Xia JX, Qiu JX, Li HM, Yuan SQ (2017) Photoelectrochemical monitoring of 4-chlorophenol by plasmonic Au/graphitic carbon nitride composites. Sens Actuators B: Chem 240:308–314. https://doi.org/10.1016/j.snb.2016.08.038
26. Li HL, Gao Y, Xiong Z, Liao C, Shih K (2018) Enhanced selective photocatalytic reduction of CO_2 to CH_4 over plasmonic Au

modified g-C_3N_4 photocatalyst under UV–vis light irradiation. Appl Surf Sci 439:552–559. https://doi.org/10.1016/j.apsusc.2018.01.071

27. Mircescu NE, Oltean M, Chis V, Leopold N (2012) FTIR, FT-Raman, SERS and DFT study on melamine. Vibrational Spectroscopy 62:165–171. https://doi.org/10.1016/j.vibspec.2012.04.008
28. Fu YS, Huang T, Jia BQ, Zhu JW, Wang X (2017) Reduction of nitrophenols to aminophenols under concerted catalysis by Au/g-C_3N_4 contact system. Appl Catal B: Environ 202:430–437. https://doi.org/10.1016/j.apcatb.2016.09.051
29. Rounaghi SA, Vanpouche DEP, Eshghi H, Scudino S, Esmaeili E, Oswald S, Eckert J (2017) A combined experimental and theoretical investigation of the Al-Melamine reactive milling system: A mechanistic study towards AlN-based ceramics. J Alloy Compd 729:240–248. https://doi.org/10.1016/j.jallcom.2017.09.168
30. Zhao H, Ding XL, Zhang B, Li YX, Wang CY (2017) Enhanced photocatalytic hydrogen evolution along with byproducts suppressing over Z-scheme $Cd_xZn_{1-x}S$/Au/g-C_3N_4 photocatalysts under visible light. Sci Bull 62:602–609. https://doi.org/10.1016/j.scib.2017.03.005
31. Niu XH, Yang X, Mo ZL, Liu NJ, Guo RB, Pan Z, Liu ZY (2019) Electrochemical chiral sensing of tryptophan enantiomers by using 3D nitrogen-doped reduced grapheme oxide. Microchem Acta 186:557–2365. https://doi.org/10.1007/s00604-019-3682-4
32. Wang Y, Yao J, Li HR, Su DS, Antonietti M (2011) Highly selective hydrogenation of phenol and derivatives over Pd@Carbon nitride catalyst in aqueous media. J Am Chem Soc 133:2362–2365. https://doi.org/10.1021/ja109856y